Stoichiometry control and electronic and transport properties of pyrochlore Bi_{2}Ir_{2}O_{7} thin films

W. C. Yang, Y. T. Xie, X. Sun, X. H. Zhang, K. Park, S. C. Xue, Y. L. Li, C. G. Tao, Q. X. Jia, Y. Losovyj, H. Wang, J. J. Heremans, and S. X. Zhang

Phys. Rev. Materials **2**, 114206 — Published 21 November 2018

DOI: 10.1103/PhysRevMaterials.2.114206

Stoichiometry control, electronic and transport properties of pyrochlore $Bi_2Ir_2O_7$ thin films

W. C. Yang[1], Y. T. Xie[2], X. Sun[3], X. H. Zhang[4], K. Park,[5] S. C. Xue[3], Y. L. Li[5], C. G. Tao[5], Q.X. Jia[6, 7], Y. Losovyj[8], H. Wang[3], J. J. Heremans[5], and S. X. Zhang[1]*

1. *Department of Physics, Indiana University, Bloomington, IN 47408, USA*
2. *SZU-NUS Collaborative Innovation Center for Optoelectronic Science & Technology, International Collaborative Laboratory of 2D Materials for Optoelectronics Science and Technology of Ministry of Education, College of Optoelectronic Engineering, Shenzhen University, Shenzhen 518060, China*
3. *School of Materials Engineering, Purdue University, West Lafayette, IN 47907, USA*
4. *Department of Physics, University of Maryland, College Park, MD 20742, USA*
5. *Department of Physics, Virginia Tech, Blacksburg, VA 24061, USA*
6. *Department of Materials Design and Innovation, University at Buffalo – The State University of New York, Buffalo, NY 14260, USA*
7. *Department of Physics, Konkuk University, Seoul 143-701, Korea*
8. *Department of Chemistry, Indiana University, Bloomington, IN 47408, USA*

** sxzhang@indiana.edu*

Abstract

Synthesizing stoichiometric and epitaxial thin films of pyrochlore iridates is an essential step towards the experimental realization of unusual topological and magnetic states that are theoretically predicted in this unique spin-orbit coupled material system. Here, we report on the stoichiometry control, electronic and transport properties of pyrochlore iridate $Bi_2Ir_2O_7$ thin films grown by pulsed laser deposition. The as-grown films form a bilayer-like structure, in which the top surface is highly Ir-deficient while the bottom layer is mainly composed of iridium metal. By post-annealing the as-deposited films in IrO_2/O_2 atmosphere, we obtained more stoichiometric and homogeneous thin films through the film thickness with their lattice constant close to the bulk value. Density functional theory calculation in the bulk limit shows a fourfold degenerate Dirac node slightly below the Fermi energy at the X point, along with trivial bands around the Γ point. The projected partial density of states suggests that the states in the vicinity of the Fermi energy (-3 ~ 0 eV) mainly consist of highly hybridized Ir 5d and O 2p with minor contributions from Bi 6s and 6p, while those far below the Fermi energy (-9 ~ -3 eV) are contributed primarily

by the O bands. Transport measurements revealed a weakly-metallic behavior at higher temperatures transitioning to a weakly-insulating behavior below 150 K, and a low-temperature magnetoresistance qualitatively ascribed to multi-carrier and bandstructural effects. The transport features are influenced by a density of states sharply peaked at the Fermi energy, and by the coexistence of trivial bands with the Dirac node, as revealed by the density functional theory calculations.

I. INTRODUCTION

5d transition metal oxides (*e.g.* iridates) are correlated materials with strong spin-orbit coupling (SOC) that have attracted significant attention in recent years[1-4]. A prominent example is formed by the pyrochlore iridates $A_2Ir_2O_7$ (or A-227 with A= Bi, Y or rare-earth element), in which exotic electronic and magnetic ground states are predicted to emerge from the interplay of electron correlation, SOC and geometrical frustration[5-10]. The effective electron interaction is tunable by the A-site ion which has a strong influence on the local structure, in particular on the Ir-O-Ir bond angle[11]. For example, when the large Pr^{3+} ions occupies the A-site, the system is in a weakly interacting regime and it forms a paramagnetic semimetal with quadratic bands touching at the Brillouin zone center[12]. By increasing the effective interaction to an intermediate regime by reducing the A-site ionic radius, the system is driven into a topological Weyl semimetal state that is accompanied by a non-collinear antiferromagnetic order[5]. Further increase of electron interaction opens up an energy gap, leading to a magnetic Mott insulator. Experimentally, the quadratic-band-touching phase has been confirmed in bulk Pr-227 crystals of weak interaction by angle-resolved photoemission spectroscopy measurement[13]; however, *direct* detection of the more exotic Weyl semimetal states in the intermediate regime remains elusive[14], although optical conductivity studies have revealed gapless features[15, 16]. A speculation is that the

Weyl semimetal states exist only in a very narrow window of interaction[17] which may be hard to controllably access in bulk materials.

Epitaxial thin films provide excellent opportunities to explore novel topological and magnetic states. First, the composition can be well controlled and tuned in most of the thin film growth process, which is essential to the experimental realization of the theoretically predicted phases in real materials, especially when the access window is narrow. Second, epitaxial growth of thin films on lattice-mismatched substrates can create lattice strains in the films, or the substrate and film can deliberately be subject to controllable stress by gluing to a piezoelectric element. In both cases, strain provides another means of symmetry breaking or tunes the effective electron interaction and hence the ground states. Indeed, recent studies on thin films of the Ruddlesden-Popper iridates (*e.g.* Sr_2IrO_4 and $SrIrO_3$) have shown remarkable influence of elastic strains on their electronic structures and magnetic properties[18-26]. Third, pyrochlore iridate films in the ultra-thin (i.e., two-dimensional) limit break the cubic symmetry and could exhibit emergent topological properties such as quantized Hall effect[17, 27-30]. Finally, thin films are ideal platforms for fabricating complex device structures including heterostructures for both the fundamental study of interface physics and the realization of practical applications.

In spite of promising features discussed above, the synthesis of pyrochlore iridate thin films has turned out to be challenging. Most of the successful growths (*e.g.,* Eu-227and Nd-227) so far have utilized a solid-phase epitaxy method, in which amorphous films were first deposited by pulsed laser deposition (PLD) or sputtering at a relatively low temperature and were then crystallized by post annealing at an elevated temperature[31-36]. To promote epitaxy, one must ensure that the nucleation occurs exclusively at the film-substrate interface in the annealing process. These films have shown electrical transport properties (*e.g.,* temperature dependence of

resistivity) that are notably different from that of the bulk crystals[31, 34, 35]. While elastic strain may play an important role on the physical properties[35], the influence of stoichiometry has yet been ruled out[31, 34]. On the other hand, epitaxial thin films of the pyrochlore iridate Bi-227 were also grown directly by PLD at a relatively high temperature[37, 38]. Interesting transport characteristics including linear positive magnetoresistance and weak-antilocalization were observed[37, 38]. Yet, chemical compositional analysis has suggested that the films are highly Ir- and oxygen-deficient[38]. In this paper, we report on the stoichiometry control of epitaxial Bi-227 thin films via a novel post annealing approach. The as-grown films form a bilayer-like structure, in which the top surface is highly Ir-deficient while the bottom layer is mainly composed of iridium metal. By post annealing the as-grown films in IrO_2/O_2 atmosphere, we realized near stoichiometric and much more homogeneous films through the film thickness with their lattice constant close to the bulk value. Density functional theory (DFT) calculations on Bi-227 in the bulk limit show a fourfold degenerate Dirac node slightly below the Fermi energy E_F at the X point, in contrast to the quadratic bands touching at the Γ point in Pr-227[12]. The DFT calculations also reveal a small sharp peak in the total density of states (DOS) at E_F, which is of importance to interpret the electronic transport measurements discussed below. The low density of carriers and concomitant reduced screening lead to a weakly-metallic behavior at higher temperatures T transitioning to a weakly-insulating behavior below 150 K, as revealed in transport measurements. While a chiral anomaly could not be detected, transport measurements showed a low-T magnetoresistance that could be understood in the framework of multi-carrier and bandstructural effects. The dependence on T and magnetic field B revealed in electronic transport reflects the influence of the coexistence of the Dirac node with trivial bands in the

vicinity of E_F, and of a DOS sharply peaked at E_F, both discerned as well in the DFT calculations.

II. EXPERIMENTAL AND CALCULATION METHODS

Bi-227 thin films were deposited on yttria-stabilized zirconia (YSZ) (111) substrates using pulsed laser deposition at a laser repetition rate of 2 Hz. The PLD target was prepared through a solid state reaction method using a mixture of IrO_2 and Bi_2O_3 at an Ir/Bi ratio of 3. Energy-dispersive X-ray spectroscopy (EDX) characterization of chemical composition was carried out in a scanning electron microscope (SEM, Quanta FEI). The EDX spectra obtained on the target show that the actual Ir/Bi ratio is ~5.5. The KrF laser energy was set to 150, 180, and 200 mJ, corresponding to a nominal laser fluence of ~ 5 J/cm^2, 6 J/cm^2 and 6.7 J/cm^2, respectively. The oxygen partial pressure was kept at 50 mTorr, and the substrate heater temperature was maintained at 750 ^{o}C. Post-annealing of thin films was carried out in a home-built three-zone quartz-tube furnace. IrO_2 powder was placed in zone 2, and the Bi-227 thin film was in zone 3. High purity oxygen gas flowed from zone 2 to zone 3 at a flow rate of 50 sccm. The oxygen pressure was kept at 300 Torr during the annealing process. The zone 2 was first heated to 1000 ^{o}C at a ramp rate of 50 ^{o}C/min, after which the temperature of the zone 3 was increased to ~500 ^{o}C at 50 ^{o}C/min. The two zones were then maintained at the soak temperatures for 0.5 hours, after which the furnace was naturally cooled down to room temperature.

X-ray diffraction (XRD) measurements were performed using either a Bruker D8 DISCOVER diffractometer or a PANalytical EMPYREAN diffractometer, where the Cu k_α line was selected as the incident beam. The 2θ-ω spectra were collected by a scintillation detector, and the reciprocal space mapping (RSM) scans were measured using a position sensitive detector

(Vantec). The RSM data were analyzed and plotted using Python. The cross-sectional samples for transmission electron microscopy (TEM) analysis were prepared via mechanical grinding, dimpling, and a low-energy ion polishing step (PIPS 691, Gatan, Inc.). The TEM, scanning transmission electron microscopy (STEM), and electron-dispersive X-ray spectroscopy (EDX) analysis were conducted using a FEI TALOS F200X at 200 kV, equipped with ultrahigh resolution high angle annular dark field detectors, and super-X EDX. Scanning tunneling microscopy (STM) characterizations were carried out in an ultrahigh vacuum STM (Omicron) system with a base pressure of 5.5×10^{-10} Torr at room temperature. The STM tip was chemically etched tungsten. The Bi-227 sample was annealed at 200 °C at the same base pressure for 3 hours before STM measurements. Atomic force microscopy (AFM) measurements were carried out on a Dimension Icon (Bruker Corporation) instrument. Scanasyst-Air cantilevers (NCST, NANO WORLD) with a spring constant of 0.4 N/m, normal resonance frequencies 70 kHz, and nominal tip radius of 2 nm were employed in Scanasyst-Air mode. X-ray photoelectron spectroscopy (XPS) was carried out using a PHI (Physical Electronics) VersaProbe II instrument equipped with a focused monochromatic Al (K_α) source[38-40]. Magnetotransport measurements were performed on a microfabricated L-shape Hall bar mesa, fabricated by photolithography followed by reactive ion etching in BCl_3 (Supplemental Material, Fig. S1[41]). The L-shape allowed the characterization of anisotropic transport properties. The active region of the Hall bar featured a length of 160 μm length and a width of 80 μm. Magnetotransport data were obtained over 1.3 K < T < 297 K in systems allowing different orientation of B *w.r.t* the film plane. Excitation currents varied between 1 μA to 1 mA, depending on measurement temperature.

DFT calculations were performed on Bi-227 in the pyrochlore structure (space group 227, Fd-3m), by using VASP[42, 43]. The generalized gradient approximation[44] and projector-augmented

wave pseudopotentials[45] were employed, and the spin-orbit coupling was included self-consistently within DFT formalism. For the calculation of band structure and density of states (DOS), we considered a face-centered cubic primitive unit cell consisting of 22 atoms with the experimental lattice constant of 10.311 Å[46], and used an energy cutoff of 400 eV and 9×9×1 *k*-point mesh. The structure was found to not carry any net magnetization.

III. RESULTS AND DISCUSSION

The Bi-227 thin films obtained using a laser fluence of ~ 5 J/cm^2 were epitaxially grown on the YSZ (111) substrate but showed significant off-stoichiometry. As shown in Fig. 1(a), only the (111) family of film peaks were observed in the XRD θ-2θ scan, indicating a (111)-oriented growth. A fine scan exhibits clear oscillations around the (222) peak of the thin film [inset of Fig. 1(a)], revealing high crystalline quality and smooth surface. The out-of-plane lattice constants d_{222} of these as-grown films were calculated to be 3.01~3.02Å, about 1% larger than that of the stoichiometric bulk sample (~ 2.98Å) [46, 47]. This out-of-plane elongation is ascribed to both off-stoichiometry and in-plane compression of the thin films. Indeed, our EDX characterization suggests a low Ir/Bi ratio of 0.55~0.65 in the as-grown films. Since Bi^{3+} has a larger ionic radius than Ir^{4+} [48], the replacement of Ir by Bi can result in an overall lattice expansion. Furthermore, as the lattice constant of Bi-227 is larger than that of the YSZ substrate, an in-plane compressive strain (and hence out-of-plane elongation) is expected as a result of epitaxial growth, which is confirmed via reciprocal space mapping of the [202] peak. As depicted in Fig. 1(b), the film peak lies below the full relaxation line of the cubic structure, indicating that the in-plane lattice of the thin film (along the x-direction) is indeed compressed while the out-of-plane (along the z-direction) is elongated. In comparison to the films grown

using a lower laser fluence of ~3.3 J/cm^2 [38], both the Ir/Bi ratio and the out-of-plane lattice constant in this work are closer to the bulk values. Further increase of laser fluence reduces the lattice constant and increases the Ir/Bi ratio (Supplemental Material, Fig. S2[41]). Yet, XRD θ-2θ measurement shows Ir metal peaks in the films grown with a high laser fluence of ~ 6 and ~ 6.7 J/cm^2. Therefore, the following discussions will focus on the films grown at a laser fluence of ~5 J/cm^2 unless otherwise noted.

A typical cross-sectional HR-TEM image [Fig. 2(a)] of the film/substrate interface area exhibits clear lattice fringes in the film, suggesting high crystallinity of the sample. The corresponding selected-area ED pattern [Fig. 2(b)] reveals well-distinguished diffraction dots similar to the ones from the substrate [Fig. 2(c)], confirming the high epitaxial quality of the film on the substrate. The epitaxial relationships of the film and the substrate are determined to be (222)Bi-227||(111)YSZ and $[02\bar{2}]$Bi-227||$[01\bar{1}]$YSZ. The matched lattice fringes and high quality epitaxial growth are also evidenced in the high resolution STEM image in Fig. 2(d). It is noted that the HR-TEM image [Fig. 2 (a)] shows a thin dark layer near the film-substrate interface suggesting the growth of a thin disordered layer at the early stage of deposition. Such disordered interface region is also obvious in the STEM image (Fig. 2(d)), revealed as a bright contrast layer, indicating a higher average atomic number Z. The EDX mapping in Fig. 2(g) suggests that the interface layer (~2.5 nm) is highly Ir-rich, while the bulk part of the film appears more uniform. The interface layer also has minimal Bi and O signals [Fig. 2(f) and (h)], indicating the formation of a metal Ir layer. It is worth noting that Ir nanocrystals were also observed in Nd-227 thin films grown by solid state epitaxy[33]. The absence of obvious Ir peaks in the XRD θ-2θ measurement [Fig. 1(a)] suggests that the Ir metal layer is very thin and may have very fine grain size.

A post-annealing approach was developed to realize high quality and stoichiometric thin films. Figure 3(a) depicts a schematic illustrating the annealing process: IrO_2 powder was first heated up to 1000 ^oC at which it sublimated to form vapor; the flow of oxygen gas carried the iridium oxide vapor downstream to react with the as-grown thin film at ~500 ^oC for 0.5 hour. As shown in Fig. 3(b) and its inset, the film maintains its (111) preferential orientation, and the (222) and (444) peaks shift to higher angles after annealing, indicating that the out-of-plane lattice constant is reduced. The value of d_{222} calculated using the (444) peak is 2.99Å, only ~0.3% larger than the bulk value[46, 47]. We note that misfit dislocation and strain relaxation may give rise to a change of lattice constant. To check if this is the case upon annealing, we did reciprocal space mapping of an annealed sample. As shown in Fig. 3(c), the annealed film is still under compressive in-plane strain, similar to the as-grown films [Fig. 1(b)]. The change in lattice constant is associated with the improved stoichiometry of the film after annealing. Indeed, EDX characterization at two different spots on an annealed film shows an Ir/Bi ratio of 1.0±0.2 and 1.0±0.3 (Supplemental Material, Fig. S3[41]), confirming the expected cation stoichiometry within the experimental uncertainties. The major uncertainty in the EDX is likely due to the large background signal from the bulk substrate that is underneath the film. We therefore carried out more surface-sensitive X-ray photoelectron spectroscopy (XPS) measurements on an annealed film; the Ir/Bi ratio determined from the XPS spectra was 1.038 ± 0.004 (Supplemental Material, Fig. S4[41]), which further confirms the stoichiometry of the films. The surface morphology of an annealed film was characterized by STM, and it shows a local overall surface roughness (root mean square height) of about 1.18 nm (Supplemental Material, Fig. S5[41]), which is comparable to that of the Eu-227 films grown by solid state epitaxy[31]. High crystalline quality of the annealed films is further confirmed by cross-sectional TEM [Fig. 4]. As shown in Fig.

4(b), lattice fringes are clearly seen in both the film and the substrate. The EDX mapping of the cross-sectional image in Fig. 4(d)-(f) shows a more uniform distribution of elements than in the as-grown film [Fig. 2(f)-(h)], and the Ir sub-layer was essentially diminished.

Our previous DFT calculation suggests that the point defects in the Ir-deficient films are antisite Bi_{Ir} rather than Ir vacancies[38]. These high density antisite defects were eliminated by post annealing in IrO_2/O_2 vapor, resulting in a decrease of lattice constant (again, since Ir^{4+} has a smaller ionic radius than Bi^{3+} [48]). The annealing contains three major processes: 1) creation of highly volatile IrO_3, 2) transport of IrO_3 gas phase towards the film, and 3) chemical reaction between IrO_3 and the Ir-deficient film. According to previous studies[49], the following chemical reaction: $2IrO_2\,(s)+O_2\,(g)=2IrO_3\,(g)$ occurs in the first process where the temperature is below 1100 °C. The equilibrium constant for this reaction is: $K_p = \frac{(P_{IrO3})^2}{P_{O2}}$, where P_{IrO3} and P_{O2} are the partial pressure of IrO_3 and O_2. Ccordfunke et al. determined a temperature-dependent equilibrium constant: $LogK_p = -\frac{27596}{T} + 16.902$ [49]. We therefore calculated the partial pressure of IrO_3 to be $P_{IrO3} = 0.07\ Torr$ based on T=1000 °C (or 1273 K) and $P_{O2} = 300\ Torr$. In the second process, the IrO_3 gas is transported by the carrier gas towards the thin film placed downstream in the quartz-tube reactor [Fig. 3 a]. In the third process, the IrO_3 (g) reacts with the Ir-deficient thin film, and the Ir atoms replace the Bi_{Ir} antisite defects, leaving excess Bi in vapor phase. Based on the standard Gibbs energy equations for the formation of gaseous bismuth and bismuth oxides[50], we found that the Bi_4O_6 (g) is the most stable phase among a variety of bismuth vapor species at the annealing temperature of 500 °C (or 773 K). Given that the Ir metal sub-layer near the substrate interface were significantly diminished after annealing, it is reasonable to believe that the Ir atoms in the metal layer also diffuse into the bulk of the film and replace the Bi_{Ir} antisite defects. It is worth noting that although post-annealing is involved in both

the solid state epitaxy[31-35] and our approach here, the mechanisms differ: in the former case, the annealing crystallizes an amorphous film, utilizing the single crystalline nature of the substrate as a driving force for epitaxy; in the latter (i.e. our case), the annealing tunes the stoichiometry of an as-grown, epitaxial film, without impacting its crystal structure. By controlling the annealing atmosphere, one can essentially apply our approach to other binary or ternary material systems that consist of elements with highly distinct vapor pressures, to achieve stoichiometry.

The electronic properties of the Bi-227 films were studied by DFT calculations. It is noted that most of the previous theoretical studies of electronic properties were focused on ultra-thin films that are composed of only a few trigonal/kagome atomic layers[27-30]. Since the films in this work are about 20 nm thick, which corresponds to ~ 66 atomic layers, it is here reasonable to carry out calculations in the 3-D bulk limit. Given the large ionic radius of Bi^{3+}, the electron interaction is believed to be rather weak and the Hubbard U term (on-site Coulomb repulsion) was hence set to zero. As observed in Fig. 5 (a) and (b), the electronic structure shows a fourfold degenerate Dirac node at 57 meV below E_F at the X point. This Dirac semimetallic feature is similar to that in β-cristobalite BiO_2, which has the same space group and was suggested to be a non-symmorphic Dirac semimetal with a fourfold degenerate Dirac node at the X point at E_F [51]. The linear dispersion is in contrast to the quadratic band touching in another metallic pyrochlore iridate, namely Pr-227 in which the effective electron interaction is also considered to be weak due to the large radius of Pr^{3+}. Coexisting with the Dirac nodes in Bi-227 are some trivial bands around the Γ point [Fig. 5 (a)].

The total DOS in Fig. 6(a) exhibits a small sharp peak at E_F, qualitatively consistent with previous calculations[46]. As a result, the electrical properties are anticipated to be sensitive to perturbations that can shift E_F away from the local maximum in the total DOS. The projected

partial DOS shown in Fig. 6(b) suggests that the states in the vicinity of E_F (-3 ~ 0 eV) mainly consists of Ir 5d and O 2p along with some minor contributions from Bi 6s and 6p, while those far below E_F (-9 ~ -3 eV) are contributed primarily by the O bands. The large overlap of the occupied states as well as their unoccupied counterpart (above E_F) suggests strong hybridization between these orbitals.

Finally, we studied the electronic transport properties of the annealed film, and we link the observed transport properties to the DFT calculations. The dependence on T of the sheet resistance (2D resistivity) $R_\square$ at B = 0 and the low-T magnetoresistance (MR, $R_\square$ *vs* B) were obtained on an L-shaped Hall bar mesa (Supplemental Material, Fig. S1[41]) prepared by photolithography and dry etching. The L-shaped Hall bar, aligned along perpendicular and non-equivalent crystal directions $[22\bar{4}]$Bi-227 and $[2\bar{2}0]$Bi-227, additionally allows the detection of anisotropic carrier transport properties, since a study of transport anisotropy has not received much attention in the pyrochlores. The sample displayed anisotropy, with values for $R_\square$ at B = 0 and T = 4.2 K of approximately 2750 Ω/□ in the high-resistivity direction $[22\bar{4}]$Bi-227 ($R_\square \rightarrow R_{xx}$) and 1300 Ω/□ in the low resistivity direction $[2\bar{2}0]$Bi-227 ($R_\square \rightarrow R_{yy}$). This stoichiometric film also displayed a sensitivity to cooldown protocol, leading to a variation in measured values for $R_\square$ of about 7%. The sensitivity is attributed to E_F lying at a small but sharp peak in the DOS, as inferred from the DFT calculations. A small variation in E_F can then lead to susbstantial variation in DOS at E_F, to which transport properties are sensitive.

The main panel in Fig. 7(a) depicts $R_\square = R_{xx}$ *vs* T for 4.2 K < T < 297 K obtained in the high-resistivity direction $[22\bar{4}]$Bi-227 at B = 0. A weakly-metallic behavior at high T transitions to a weakly-insulating behavior for T < 150 K. The changeover and resulting minimum in $R_\square$ *vs* T is not believed to be due to an electronic or structural transition. The weakly-insulating behavior

results only in a maximal ~ 6 % increase in sheet resistance between 150 K and 4.2 K, and is hence not as pronounced as the insulating behavior that would result from a band gap. The data (Fig. 7(a) and its inset for $B = 0$) further do not closely fit a power law $R_{\square} \sim T^{\alpha}$, in contrast to observations in bulk single crystals[46] and further do not follow $1/R_{\square} \sim \ln(T)$, as would be expected from the Aronov-Altshuler mechanism for electron-electron interactions[52-54] due to an effective suppression of the DOS at E_F. The broad minimum in sheet resistance at 150 K and the weakly-insulating behavior for $T < 150$ K are instead ascribed to the competition between decreasing scattering of carriers by phonons with decreasing T, and a progressive carrier trapping at lower T, in a disorder potential largely unscreened due to a relatively low DOS at E_F. These findings are supported by the DFT calculations. Strain in the film can also contibute to disorder, to which transport properties will be sensitive, although not necessarily detectable in TEM studies. The observed transport anisotropy along $[22\bar{4}]$Bi-227 compared to $[2\bar{2}0]$Bi-227 would not be expected for unstrained bulk crystals with cubic symmetry. Nevertheless, a transport anisotropy is regularly observed in thin films of cubic crystals. The anisotropy has not received as much attention in pyrochlores as it has in technologically important face-centered cubic semiconductors such as multivalley Si[55, 56] and Ge[57-61] or high-index GaAs[62], where the anisotropy is well-recognized and taken into account in device fabrication. The anisotropy in Si, Ge and GaAs has been attributed to effects on bandstructure carrier valleys of residual strain (resulting in an effectively uniaxial distortion) and surface effects breaking the cubic symmetry[55, 58, 60], and to anisotropic scattering (*i.e.* surface scattering, phonon scattering, intervalley scattering, or impurity scattering not conforming to the cubic symmetry)[56, 57, 59, 61, 62]. In the multivalley semiconductors the exact origin of the experimentally observed anisotropy has typically not been straightforward to discern, and likewise, the origin of the observed transport

anisotropy between [22$\bar{4}$]Bi-227 and [2$\bar{2}$0]Bi-227, while an experimental fact, has not been elucidated. In the present work, STM on the Bi-227 thin film (*cfr* Supplemental Material, Fig. S5[41]) and AFM on the YSZ substrate (*cfr* Supplemental Material, Fig. S6[41]) did not detect surface morphologies (*e.g.* ripples) that could induce anisotropic surface or interface scattering[57, 62]. Possibly, the predominantly biaxial strain originating in the film growth on YSZ substrates (as evidenced by the RSM data in Fig. 3(c)) has a residual uniaxial component breaking the cubic symmetry and contributing to the anisotropy. Anisotropic phonon scattering, intervalley scattering, or impurity scattering cannot be excluded. Further, Fig. S7 of Supplemental Material (calculated by DFT) is included to show the multivalley character of the Bi-227 around E_F [41], and the figure highlights the different energy dispersions found in the valleys along the [22$\bar{4}$]Bi-227 and [2$\bar{2}$0]Bi-227 directions. As in Si and Ge, the multivalley character likely renders Bi-227 prone to transport anisotropy due to the mechanisms enumerated above. The inset in Fig. 7(a) compares $R_{\square} = R_{xx}$ *vs* T for 1.3 K < T < 10 K, in the high-resistivity direction [22$\bar{4}$]Bi-227 for cooldowns at B = 0 and at B = 5 T (with B applied perpendicularly to the film surface). While MR is evident from the comparison, no evidence for a magnetic transition[63] is apparent in the range 1.3 K < T < 10 K.

Figure 7(b) contains measurements of MR ($R_{\square} = R_{xx}$ over -5 T < B < 5 T) in the high-resistivity direction [22$\bar{4}$]Bi-227 at different T. The traces at 4.87 K, 1.83 K, 1.55 K and 1.32 K were obtained with B applied perpendicularly to the film surface, after cooldown under B = 0. The trace at T = 1.44 K was obtained with B applied perpendicularly to the film but after cooling the sample from 10 K under perpendicular B = 5 T. The trace at T = 1.27 K was obtained (after B = 0 cooldown) with B applied in-plane and parallel to the measurement current direction, hence parallel to the electric field over the sample, to probe the presence of possible chiral anomaly,

potentially induced by lifting of the degeneracy of the Dirac node (not observed, *cfr* below). Magnetic hysteresis in the MR traces could not be observed in any of the cases, pointing to an absence of magnetic order. The gradual evolution under decreasing T apparent from the comparison of the traces obtained at 4.87 K, 1.83 K, 1.55 K and 1.32 K also argues for the absence of a magnetic transition in this range of T, as corroborated by the data in the inset of Fig. 7(a). The Aronov-Altshuler mechanism for electron-electron interactions [52-54] is not favored by the dependence of $R_{\square}$ on T at B = 0 (Fig. 7(a)) and is thereby eliminated as a source of the observed positive MR. Instead, the positive MR and its gradual dependence on T (Fig. 7(a) inset) may indicate the existence of multiple types of charge carriers, originating in the presence of multiple bands in the electronic structure [Fig. 5 and ref. [64]]. The complex bandstructure as calculated by DFT (Fig. 5), featuring a coexistence of the Dirac node with trivial bands in the vicinity of E_F, supports the contribution of multiple types of charge carriers. The MR at T = 4.87 K assumes a more pronounced linear dependence on B at higher B. A linear positive MR at high B can be due to a linear or quasi-relativistic dispersion of the underlying electronic structure (as observed in topological insulators, Bi, Dirac materials, and narrow-gap semiconductors)[65]. In the present material, the linear dispersion characteristic of the Dirac node just below E_F can contribute to the linear MR. While a detailed analysis is not emphasized in the present work, the observed MR hence appears to result from a combination of several phenomena, including multi-carrier effects and linear MR due to bandstructure, both features supported by the DFT calculations. It is also noted that the MR obtained with B applied parallel to the electric field over the sample (T = 1.27 K) does not substantially differ from the MR obtained under perpendicular B, and hence effects of a chiral anomaly [66] cannot be inferred. The inset of Fig. 7(b) depicts the MR ($R_{\square} = R_{yy}$ *vs* B) in the low-resistivity direction $[2\bar{2}0]$Bi-227, obtained at T =

1.32 K. This MR bears a strong resemblance to the MR obtained in the high-resistivity direction at 1.32 K, but is of somewhat lower relative magnitude (3% rather than 4 % over 5 T). Comparing the present thin film results for $R_{\square}$ *vs* T (Fig. 7(a)) with results on a bulk $Bi_2Ir_2O_7$ sample [46], we find that the metallic low-T dependence $R_{\square} \sim T^{3/2}$ observed in the bulk sample for 1.7 K < T < 10 K is not observed in the thin film, while Ref. [46] similarly concludes that the sensitivity of transport properties to external parameters can originate in E_F lying at a small but sharp peak in the DOS. Concerning $R_{\square}$ *vs* B (Fig. 7(b)), the bulk $Bi_2Ir_2O_7$ sample [46] lacks significant MR for $B \leq 14$ T, in contrast to the present thin-film material.

IV. CONCLUSIONS

In summary, we developed a post-annealing approach to tune the stoichiometry and lattice parameters of Bi-227 thin films grown by pulsed laser deposition. The as-grown films form a bilayer-like structure, in which the top layer is highly Ir-deficient Bi-227 while the bottom layer is mainly composed of Ir metal. By post-annealing in IrO_2 atmosphere, we realized much more stoichiometric and homogeneous thin films through the film thickness with their lattice constant close to the bulk value. The same approach may be applied to other non-stoichiometric binary or ternary material systems to control stoichiometry. DFT calculations in the bulk limit show a fourfold degenerate Dirac node slightly below the Fermi energy at the X point, coexisting with trivial bands around the Γ point. The projected partial DOS suggests that the states in the vicinity of the Fermi energy (-3 ~ 0 eV) mainly consist of highly hybridized Ir 5d and O 2p with minor contributions from Bi 6s and 6p. The states further below the Fermi energy (-9 ~ -3 eV) are contributed mainly by the O bands. Transport measurements could not detect a chiral anomaly, but showed a weakly-metallic behavior at higher temperatures transitioning to a weakly-

insulating behavior below 150 K. Transport measurements also showed a low-temperature magnetoresistance, attributed to multi-carrier and bandstructural effects.

ACKNOWLEDGEMENTS

S. X. Z. acknowledges Indiana University (IU) College of Arts and Sciences for startup support. H.W. and X. S. acknowledge the support from the U.S. National Science Foundation (DMR-1565822) for the TEM/STEM effort at Purdue University. J. J. H. and Y. T. X. were supported by the U.S. Department of Energy, Office of Basic Energy Sciences, Division of Materials Sciences and Engineering under award DOE DE-FG02-08ER46532. The authors also acknowledge the Nanoscale Characterization Facility for the use of SEM instrument and the Indiana University Molecular Structure Center for XRD facility (NSF Grant No. 400 CHE-1048613).

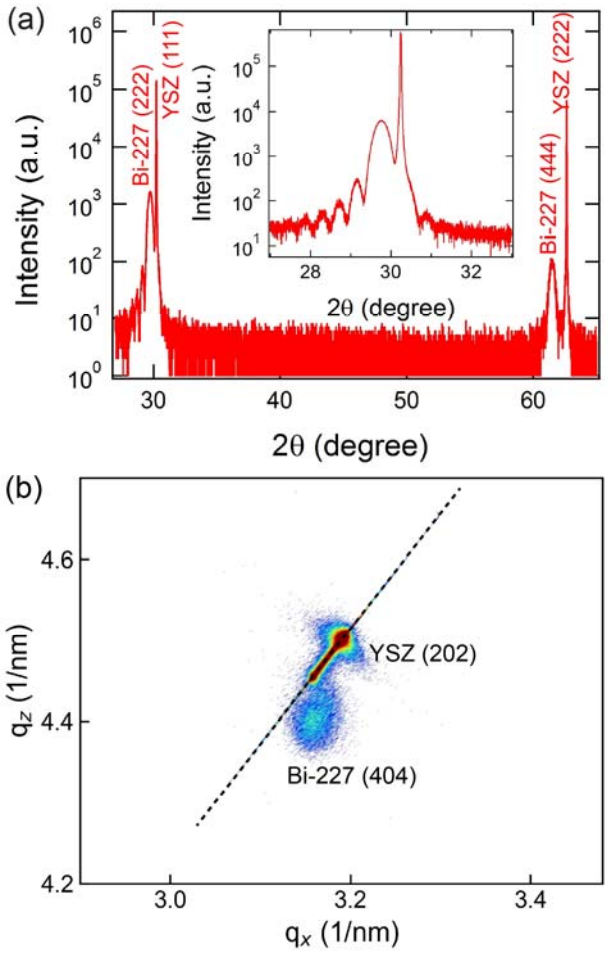

Figure 1. (a) X-ray diffraction θ-2θ scan of a Bi-227 thin film grown on YSZ (111) using a laser fluence of ~ 5 J/cm^2. The inset shows a fine scan around the (222) peak of the film. (b) Reciprocal space mapping around the YSZ (202) peak. The intensity was normalized and plotted in log scale. The dashed line extrapolates to the origin of the q_x-q_z graph and hence represents a full relaxation of the cubic structure.

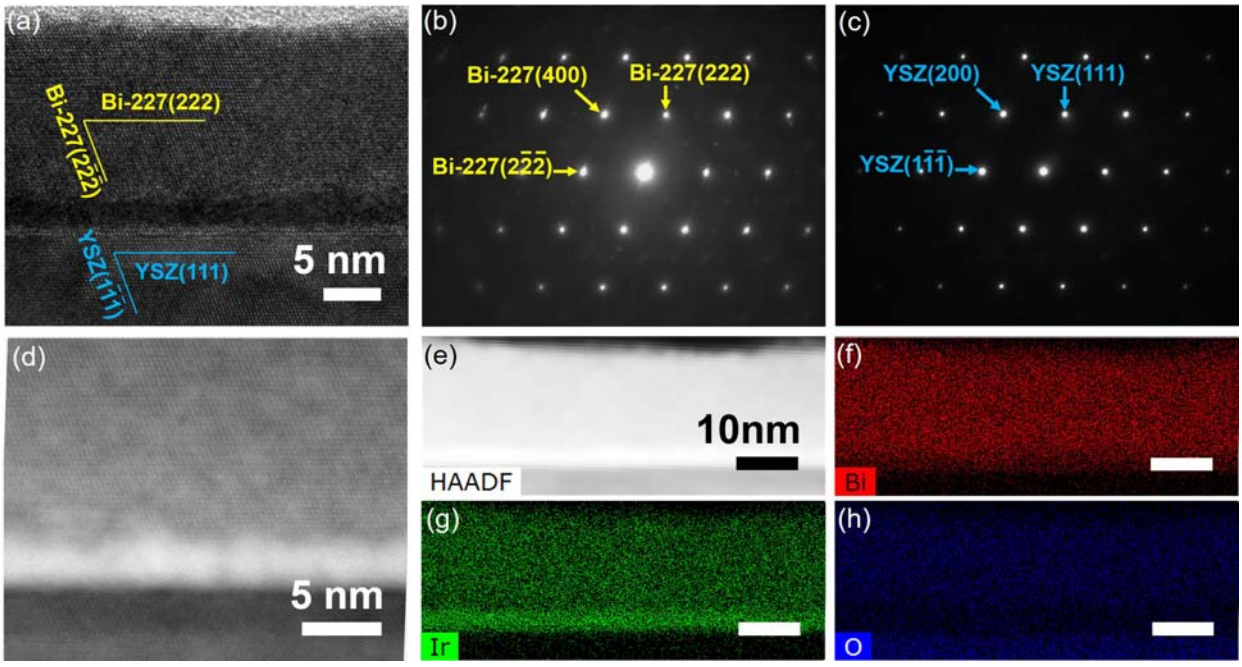

Figure 2. (a) Cross-sectional TEM image of a Bi-227 film grown on YSZ (111) substrate. Selected-area electron diffraction pattern taken from (b) the thin film and (c) the YSZ substrate region. (d) High resolution STEM image showing clear lattice fringes of the film and the substrate. e) STEM image of the thin film and the corresponding EDX mapping of the elements of (f) Bi, (g) Ir and (h) O.

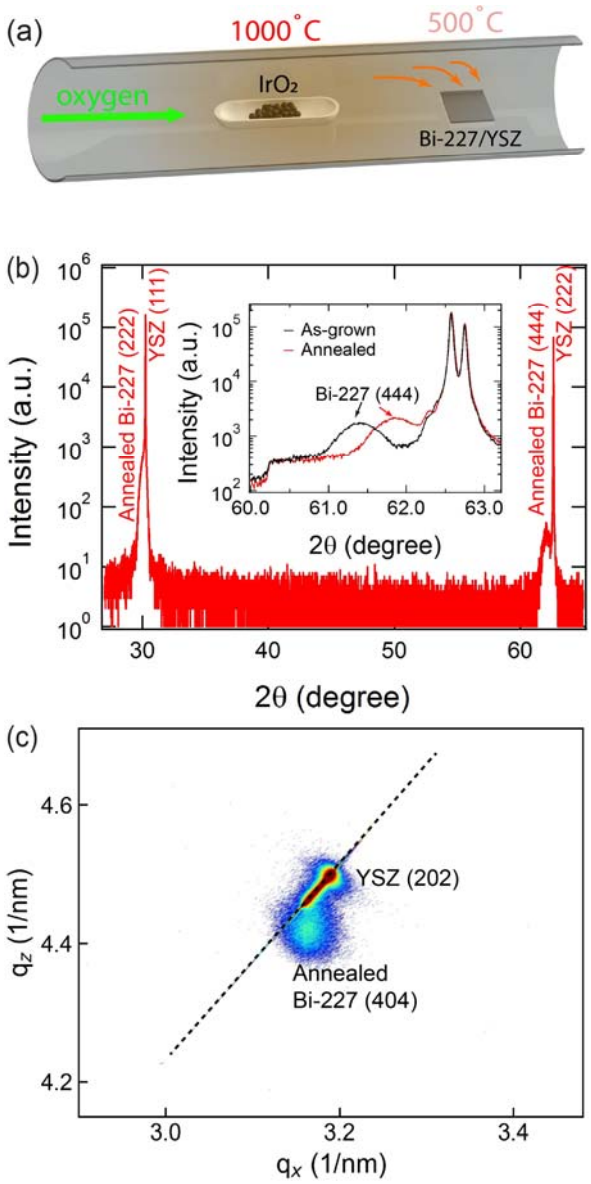

Figure 3. (a) A schematic picture showing the annealing process. (b)XRD θ-2θ scan of an annealed sample; the inset shows fine scans around the (444) peak of the film taken using a PANalytical EMPYREAN diffractometer. The two patterns were calibrated using the YSZ substrate peak, and their intensities were normalized for a better comparison of the film peak positions. (c) Reciprocal space mapping around the YSZ (202) peaks. The intensity was normalized and plotted in log scale. The dashed line extrapolates to the origin of the q_x-q_z graph and hence represents a full relaxation of the cubic structure.

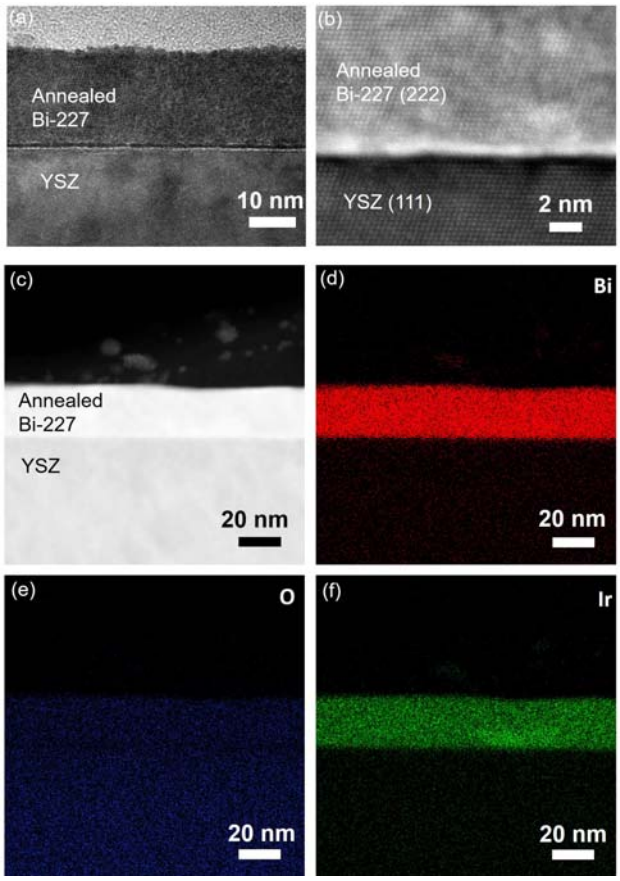

Figure 4. (a) Cross-sectional TEM image, (b) Scanning TEM, and EDX mapping of (d) Bi, (e) O and (f) Ir of an annealed Bi-227 thin film. A slight variation of thickness was observed in different sample regions.

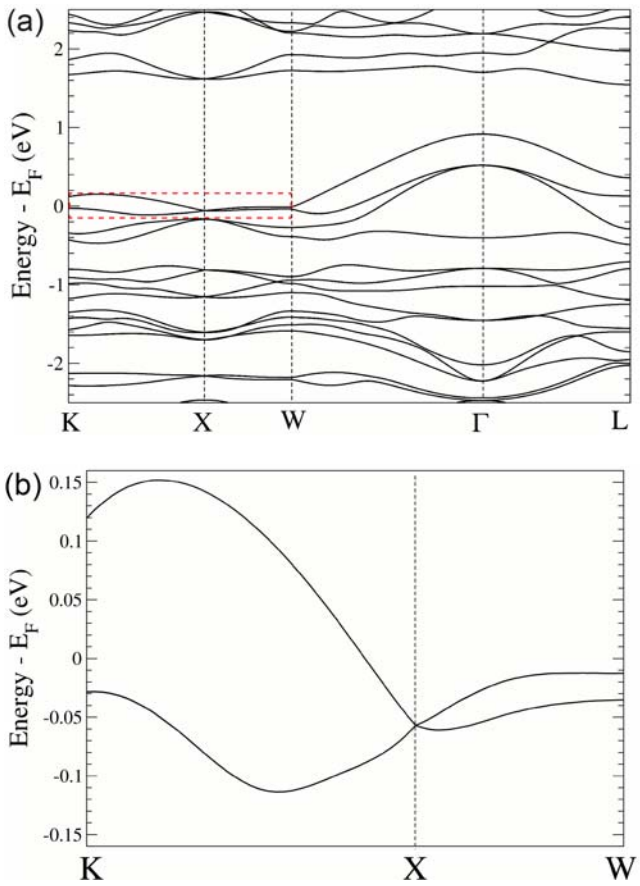

Figure 5. (a) Electronic band structure of Bi-227 calculated using DFT, where energies are referred relative to the Fermi energy E_F. (b) Electronic band structure zoomed in near the Dirac node at the X point (as denoted by the box in (a)).

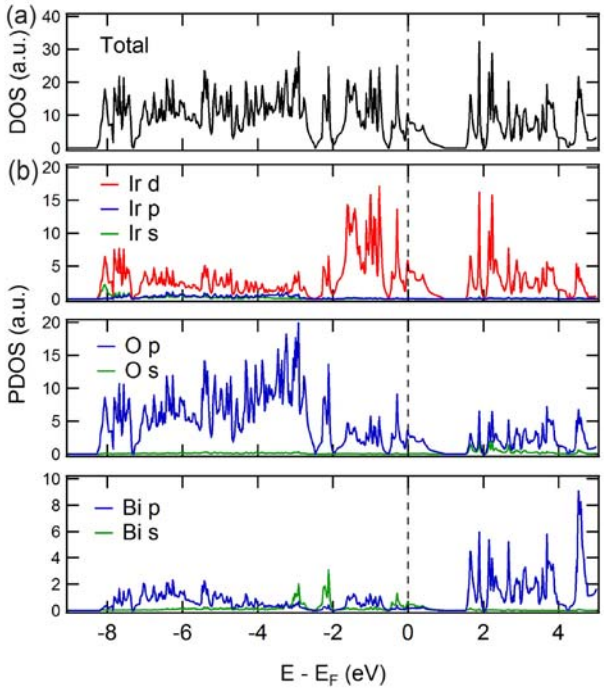

Figure 6. (a) Total density of states and (b) projected partial density of states onto the orbitals for Bi-227 calculated using DFT. Energies are referred relative to E_F (dashed lines).

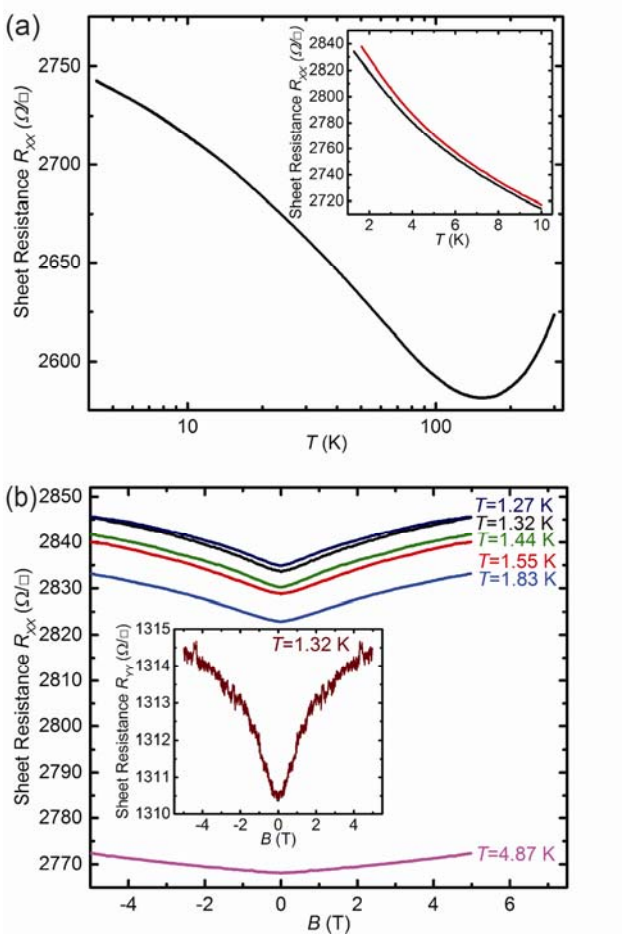

Figure 7. (a) Sheet resistance $R_{\square}$ *vs* T at $B = 0$ in the high-resistivity direction $[22\bar{4}]$Bi-227 ($R_{\square} = R_{xx}$). The inset shows $R_{\square} = R_{xx}$ *vs* T under $B = 0$ (black curve) and under $B = 5$ T applied perpendicularly to the film surface (red curve) in the high-resistivity direction $[22\bar{4}]$Bi-227, for 1.3 K < T < 10 K. Due to the sensitivity to cooldown protocol, a slight variation in sheet resistance (a few %) is noted at the same T for different traces. (b) Magnetoresistance $R_{\square} = R_{xx}$ *vs* B at indicated T in the high-resistivity direction $[22\bar{4}]$Bi-227. The traces are obtained under different field conditions are as explained in the text. The inset shows the magnetoresistance $R_{\square} = R_{yy}$ *vs* B at 1.32 K in the low-resistivity direction $[2\bar{2}0]$Bi-227, after cooldown to ~ 1.30 K at $B = 0$.

References

1. W. Witczak-Krempa, G. Chen and Y. B. Kim, Annual Review of Condensed Matter Physics **5**, 57-82 (2013).
2. R. Schaffer, E. K. H. Lee, B. J. Yang and Y. B. Kim, Rep Prog Phys **79**, 094504 (2016).
3. J. G. Rau, E. K. H. Lee and H. Y. Kee, Annu Rev Conden Ma P **7**, 195-221 (2016).
4. G. Cao and P. Schlottmann, Rep Prog Phys **81**, 042502 (2018).
5. X. G. Wan, A. M. Turner, A. Vishwanath and S. Y. Savrasov, Phys Rev B **83**, 205101 (2011).
6. D. Pesin and L. Balents, Nat Phys **6**, 376 (2010).
7. K. Y. Yang, Y. M. Lu and Y. Ran, Phys Rev B **84**, 075129 (2011).
8. W. Witczak-Krempa and Y. B. Kim, Phys Rev B **85**, 045124 (2012).
9. M. Kargarian, J. Wen and G. A. Fiete, Phys Rev B **83**, 165112 (2011).
10. Y. Machida, S. Nakatsuji, S. Onoda, T. Tayama and T. Sakakibara, Nature **463**, 210-213 (2010).
11. H. J. Koo, M. H. Whangbo and B. J. Kennedy, J Solid State Chem **136** (2), 269-273 (1998).
12. E. G. Moon, C. K. Xu, Y. B. Kim and L. Balents, Phys Rev Lett **111**, 206401 (2013).
13. T. Kondo, M. Nakayama, R. Chen, J. J. Ishikawa, E. G. Moon, T. Yamamoto, Y. Ota, W. Malaeb, H. Kanai, Y. Nakashima, Y. Ishida, R. Yoshida, H. Yamamoto, M. Matsunami, S. Kimura, N. Inami, K. Ono, H. Kumigashira, S. Nakatsuji, L. Balents and S. Shin, Nat Commun **6**, 10042 (2015).
14. M. Nakayama, T. Kondo, Z. Tian, J. J. Ishikawa, M. Halim, C. Bareille, W. Malaeb, K. Kuroda, T. Tomita, S. Ideta, K. Tanaka, M. Matsunami, S. Kimura, N. Inami, K. Ono, H. Kumigashira, L. Balents, S. Nakatsuji and S. Shin, Phys Rev Lett **117**, 056403 (2016).
15. K. Ueda, J. Fujioka, Y. Takahashi, T. Suzuki, S. Ishiwata, Y. Taguchi and Y. Tokura, Phys Rev Lett **109** (13), 136402 (2012).
16. A. B. Sushkov, J. B. Hofmann, G. S. Jenkins, J. Ishikawa, S. Nakatsuji, S. Das Sarma and H. D. Drew, Phys Rev B **92**, 241108 (R) (2015).
17. K. Hwang and Y. B. Kim, Sci Rep-Uk **6**, 30017 (2016).
18. C. R. Serrao, J. Liu, J. T. Heron, G. Singh-Bhalla, A. Yadav, S. J. Suresha, R. J. Paull, D. Yi, J. H. Chu, M. Trassin, A. Vishwanath, E. Arenholz, C. Frontera, J. Zelezny, T. Jungwirth, X. Marti and R. Ramesh, Phys Rev B **87**, 085121 (2013).
19. J. Nichols, J. Terzic, E. G. Bittle, O. B. Korneta, L. E. De Long, J. W. Brill, G. Cao and S. S. A. Seo, Appl Phys Lett **102**, 141908 (2013).
20. J. Nichols, O. B. Korneta, J. Terzic, L. E. De Long, G. Cao, J. W. Brill and S. S. A. Seo, Appl Phys Lett **103**, 131910 (2013).
21. L. D. Miao, H. Xu and Z. Q. Mao, Phys Rev B **89**, 035109 (2014).
22. A. Lupascu, J. P. Clancy, H. Gretarsson, Z. X. Nie, J. Nichols, J. Terzic, G. Cao, S. S. A. Seo, Z. Islam, M. H. Upton, J. Kim, D. Casa, T. Gog, A. H. Said, V. M. Katukuri, H. Stoll, L. Hozoi, J. van den Brink and Y. J. Kim, Phys Rev Lett **112**, 147201 (2014).
23. N. Domingo, L. Lopez-Mir, M. Paradinas, V. Holy, J. Zelezny, D. Yi, S. J. Suresha, J. Liu, C. R. Serrao, R. Ramesh, C. Ocal, X. Marti and G. Catalan, Nanoscale **7**, 3453-3459 (2015).
24. L. Y. Zhang, Q. F. Liang, Y. Xiong, B. B. Zhang, L. Gao, H. D. Li, Y. B. Chen, J. Zhou, S. T. Zhang, Z. B. Gu, S. H. Yao, Z. M. Wang, Y. Lin and Y. F. Chen, Phys Rev B **91**, 035110 (2015).
25. B. Kim, B. H. Kim, K. Kim and B. I. Min, Sci Rep-Uk **6**, 27095 (2016).

26. X. R. Liu, Y. W. Cao, B. Pal, S. Middey, M. Kareev, Y. Choi, P. Shafer, D. Haskel, E. Arenholz and J. Chakhalian, Phy Rev Mater **1**, 075004 (2017).
27. B. J. Yang and N. Nagaosa, Phys Rev Lett **112**, 246402 (2014).
28. X. Hu, A. Rüegg and G. A. Fiete, Phys Rev B **86**, 235141 (2012).
29. X. Hu, Z. C. Zhong and G. A. Fiete, Sci Rep-Uk **5**, 11072 (2015).
30. Q. Chen, H. H. Hung, X. Hu and G. A. Fiete, Phys Rev B **92**, 085145 (2015).
31. T. C. Fujita, Y. Kozuka, M. Uchida, A. Tsukazaki, T. Arima and M. Kawasaki, Sci Rep-Uk **5**, 9711 (2015).
32. T. C. Fujita, M. Uchida, Y. Kozuka, W. Sano, A. Tsukazaki, T. Arima and M. Kawasaki, Phys Rev B **93**, 064419 (2016).
33. J. C. Gallagher, B. D. Esser, R. Morrow, S. R. Dunsiger, R. E. A. Williams, P. M. Woodward, D. W. McComb and F. Y. Yang, Sci Rep-Uk **6**, 22282 (2016).
34. Y. Kozuka, T. C. Fujita, M. Uchida, T. Nojima, A. Tsukazaki, J. Matsuno, T. Arima and M. Kawasaki, Phys Rev B **96**, 224417 (2017).
35. T. Ohtsuki, Z. Tian, A. Endo, M. Halim, S. Katsumoto, Y. Kohama, K. Kindo, S. Nakatsuji and M. Lippmaa, arXiv:1711.07813 (2017).
36. T. C. Fujita, Y. Kozuka, J. Matsuno, M. Uchida, A. Tsukazaki, T. Arima and M. Kawasaki, Phy Rev Mater **2**, 011402(R) (2018).
37. J.-H. Chu, S. C. Riggs, M. Shapiro, J. Liu, C. R. Serero, D. Yi, M. Melissa, S. J. Suresha, C. Frontera, A. Vishwanath, X. Marti, I. R. Fisher and R. Ramesh, arXiv **1309.4750v2** (2013).
38. W. C. Yang, Y. T. Xie, W. K. Zhu, K. Park, A. P. Chen, Y. Losovyj, Z. Li, H. M. Liu, M. Starr, J. A. Acosta, C. G. Tao, N. Li, Q. X. Jia, J. J. Heremans and S. X. Zhang, Sci Rep-Uk **7**, 7740 (2017).
39. Z. Li, E. Z. Xu, Y. Losovyj, N. Li, A. P. Chen, B. Swartzentruber, N. Sinitsyn, J. Yoo, Q. X. Jia and S. X. Zhang, Nanoscale **9**, 13014-13024 (2017).
40. E. Z. Xu, H. M. Liu, K. Park, Z. Li, Y. Losovyj, M. Starr, M. Werbianskyj, H. A. Fertig and S. X. Zhang, Nanoscale **9**, 3576-3584 (2017).
41. See Supplemental Material at [URL will be inserted by publisher] for Hall device fabrication and geometry, influence of laser fluence on film composition and lattice constant, EDX, XPS, and STM characterizations of thin films, AFM characterization of YSZ substrate, Density-functional-theory calculation of the electronic bandstructure
42. G. Kresse and J. Furthmuller, Phys Rev B **54**, 11169 (1996).
43. G. Kresse and J. Furthmuller, Comp Mater Sci **6**, 15-50 (1996).
44. J. P. Perdew, K. Burke and M. Ernzerhof, Phys Rev Lett **77**, 3865 (1996).
45. P. E. Blochl, Phys Rev B **50**, 17953 (1994).
46. T. F. Qi, O. B. Korneta, X. Wan, L. E. DeLong, P. Schlottmann and G. Cao, J Phys-Condens Mat **24**, 345601 (2012).
47. Y. S. Lee, S. J. Moon, S. C. Riggs, M. C. Shapiro, I. R. Fisher, B. W. Fulfer, J. Y. Chan, A. F. Kemper and D. N. Basov, Phys Rev B **87**, 195143 (2013).
48. R. D. Shannon, Acta Crystallogr A **32**, 751-767 (1976).
49. E. H. P. Cordfunke and G. Meyer, Recl Trav Chim Pay B **81**, 495 (1962).
50. S. C. Marschman and D. C. Lynch, Can J Chem Eng **62**, 875-879 (1984).
51. S. M. Young, S. Zaheer, J. C. Y. Teo, C. L. Kane, E. J. Mele and A. M. Rappe, Phys Rev Lett **108**, 140405 (2012).
52. P. A. Lee and T. V. Ramakrishnan, Rev Mod Phys **57**, 287 (1985).
53. R. S. Markiewicz and C. J. Rollins, Phys Rev B **29**, 735-747 (1984).

54. B. L. Altshuler and A. G. Aronov, Solid State Commun **30** (3), 115-117 (1979).
55. R. F. Pierret and C. T. Sah, Solid State Electron **11**, 279 (1968).
56. M. V. Fischetti, Z. Ren, P. M. Solomon, M. Yang and K. Rim, J Appl Phys **94**, 1079-1095 (2003).
57. A. H. A. Hassan, R. J. H. Morris, O. A. Mironov, R. Beanland, D. Walker, S. Huband, A. Dobbie, M. Myronov and D. R. Leadley, Appl Phys Lett **104**, 132108 (2014).
58. Y. I. Gorkun, V. S. Lysenko, V. G. Litovchenko and V. A. Novominskii, Physica Status Solidi a-Applications and Materials Science **3**, K281-K284 (1970).
59. C. Morrison and M. Myronov, Appl Phys Lett **111**, 192103 (2017).
60. S. Dissanayake, Y. Zhao, S. Sugahara, M. Takenaka and S. Takagi, J Appl Phys **109**, 033709 (2011).
61. V. Aubry-Fortuna and P. Dollfus, J Appl Phys **108**, 123706 (2010).
62. J. J. Heremans, M. B. Santos, K. Hirakawa and M. Shayegan, J Appl Phys **76**, 1980-1982 (1994).
63. P. J. Baker, J. S. Möller, F. L. Pratt, W. Hayes, S. J. Blundell, T. Lancaster, T. F. Qi and G. Cao, Phys Rev B **87**, 180409(R) (2013).
64. Q. Wang, Y. Cao, X. G. Wan, J. D. Denlinger, T. F. Qi, O. B. Korneta, G. Cao and D. S. Dessau, Journal of Physics-Condensed Matter **27**, 015502 (2015).
65. M. Veldhorst, M. Snelder, M. Hoek, C. G. Molenaar, D. P. Leusink, A. A. Golubov, H. Hilgenkamp and A. Brinkman, Phys Status Solidi-R **7**, 26-38 (2013).
66. E. Barnes, J. J. Heremans and D. Minic, Phys Rev Lett **117**, 217204 (2016).